RSC Advances

PAPER

Cite this: *RSC Adv.*, 2025, **15**, 1323

Unveiling the physicochemical, photocatalytic, antibacterial and antioxidant properties of MWCNT-modified Ag_2O/CuO/ZnO nanocomposites

Amjad Latif Lone,[a] Sadiq Ur Rehman,*[a] Sirajul Haq,*[a] Nadia Shahzad,[b] Mohammad Khalid Al-Sadoon,[c] Muhammad Imran Shahzad,[d] Jamoliddin Razzokov,[efg] Shafia Shujaat[a] and Abdus Samad[h]

Water pollution, oxidative stress and the emergence of multidrug-resistant bacterial strains are significant global threats that require urgent attention to protect human health. Nanocomposites that combine multiple metal oxides with carbon-based materials have garnered significant attention due to their synergistic physicochemical properties and versatile applications in both environmental and biomedical fields. In this context, the present study was aimed at synthesizing a ternary metal-oxide nanocomposite consisting of silver oxide, copper oxide, and zinc oxide (ACZ-NC), along with a multi-walled carbon nanotubes modified ternary metal-oxide nanocomposite (MWCNTs@ACZ-NC). The properties of the synthesized nanomaterials were characterized using Fourier transform infrared (FT-IR) spectroscopy, field emission scanning electron microscopy (FESEM), X-ray diffraction (XRD), and energy dispersive X-ray (EDX) spectroscopy. The results obtained suggested the successful synthesis of both samples, as evidenced by the morphological changes observed in the SEM images, a transmittance band at 748.02 cm^{-1} in the FT-IR spectrum, and a diffraction peak at 44.39° in the XRD pattern. The band gap energies were determined *via* diffuse reflectance spectroscopy (DRS), with a redshift observed in the absorbance edge upon the incorporation of MWCNTs. The synthesized samples were tested as photocatalysts for the degradation of rhodamine 6G (Rh-6G), with the highest degradation efficiency (99.61%) achieved by MWCNTs@ACZ-NC. Additionally, the materials were evaluated for their biological activity as antibacterial and antioxidant agents. The MWCNTs@ACZ-NC exhibited the highest antioxidant potential with an IC_{50} value of 59.22 μg mL^{-1}. However, the incorporation of MWCNTs resulted in a decrease in antibacterial activity, which may be attributed to the blocking of binding sites.

Received 1st December 2024
Accepted 27th December 2024

DOI: 10.1039/d4ra08466g

rsc.li/rsc-advances

1. Introduction

Over the past few years, concerns about the impacts of environmental pollution on public health have intensified, particularly regarding water pollution caused by industrialization and unregulated human activities. A large number of people worldwide lack access to safe drinking water due to pollutants, such as heavy metals, dyes, and chemicals contaminating water bodies.[1,2] Organic dyes, such as Rh-6G, which are used in various applications, significantly contribute to water pollution and pose risks to human health, including allergic reactions. While numerous methods, such as biological, chemical, and physical processes, exist to remove organic dyes from wastewater, these approaches can be costly and inefficient, often generating substantial sludge. The photocatalytic process, first introduced in 1911, offers a more effective, cost-efficient, and environmentally friendly alternative for treating water pollution.

Antioxidants are compounds that inhibit oxidation reactions by scavenging free radicals and converting them into stable, non-reactive molecules.[3] The imbalance between the excessive formation of oxidants and the ability of antioxidant defense mechanisms to scavenge them results in a pathophysiological condition known as oxidative stress. In this condition, the levels

[a]*Department of Chemistry, University of Azad Jammu and Kashmir, Muzaffarabad 13100, Pakistan. E-mail: srkhattak@hotmail.com; cii_raj@yahoo.com*
[b]*US–Pakistan Centre for Advanced Studies in Energy, National University of Science and Technology (NUST), 44000 Islamabad, Pakistan*
[c]*Department of Zoology, College of Science, King Saud University, P. O. Box 2455, Riyadh, 11451, Saudi Arabia*
[d]*Nanosciences and Technology Department (NS & TD), National Center for Physics (NCP), 44000 Islamabad, Pakistan*
[e]*Institute of Fundamental and Applied Research, National Research University TIIAME, Kori Niyoziy 39, 100000 Tashkent, Uzbekistan*
[f]*Alfraganus University, Yukori Karakamish street 2a, 100190 Tashkent, Uzbekistan*
[g]*Department of Biotechnology, Tashkent State Technical University, Universitet 2, Tashkent 100095, Uzbekistan*
[h]*School of Material Science and Engineering, Nanjing Tech University, P. R China*

of reactive nitrogen species (such as peroxynitrite) as well as reactive oxygen species (including hydroxyl radicals, atomic oxygen, and superoxide anions) increase.[4] When RNS and ROS are produced in excess, they can damage DNA, proteins, and cellular and subcellular membranes by interacting with them, impairing their normal functions. This can lead to various diseases, such as aging,[5] neurodegenerative disorders,[6] cardiovascular diseases, diabetes, asthma, pulmonary conditions[7] and cancer.[8] To counteract the effects of oxidative stress, both synthetic and natural antioxidants are used. Besides natural antioxidants, there is a precise need to develop effective synthetic antioxidants that not only overcome the adverse activity of oxidants but also help in retaining the normal functions of the damaged cells. Among nanomaterials, metal-oxide nanoparticles (MO-NPs) are very reactive particles because of the unpaired valence shell electrons present on their surfaces.[9] Therefore, clinical applications of these NPs have more advantages over the conventional therapy treatments, which have numerous side effects and problems of reduced efficiency at target sites. MO-NPs have been investigated for many biological applications such as antimicrobial, antioxidant, drug delivery, bioimaging and biosensing.[10]

Copper oxide (CuO) is one of the important transition metal oxides having a small energy gap (nearly 2.0 eV). It exhibits good electrochemical, mechanical, and biological applications at the nanoscale.[11] Many researchers worked on the synthesis of CuO NPs and studied their antioxidant, antibacterial and photocatalytic activities.[12–14] Silver oxide (Ag_2O) NPs have gained interest due to their versatility in the field of medical science, like in drug delivery, as oxidation inhibitors, antimicrobial agents, carcinostatic substances, and inflammation reducers.[15] Studies of Ag_2O-NPs have shown that they exhibit great potential against the oxidants and other inflammatory substances; therefore, they have been investigated as antioxidant and antibacterial agents by many researchers.[16–18] Zinc oxide (ZnO) nanocrystals have gained particular interest due to their 3.37 eV band gap and their ability to act as n-type semiconductors.[19] Zn is an essential element in the body; although it is required in minute quantities, it plays an important role in enzymatic activities during the synthesis of nucleic acid and proteins. ZnO is a non-toxic and environmentally friendly material that actively participates in combating cancerous and inflammatory cells.[20] Photocatalytic, antibacterial and antioxidant potentials of ZnO-NPs have been explored by many researchers in the recent past.[21–23] Carbon nanotubes (CNTs) are a major class of nanostructured organic compounds. They are one-dimensional materials having a high aspect ratio.[24] CNTs fall into two categories: single-walled CNTs as well as multi-walled CNTs. CNTs have drawn attraction in last decade in the fields of biology and pharmaceutics; hence, the modified CNTs have now diverse applications in nucleic acid sequencers, biocatalysts and biological processes.[25] This research explores the potential of functionalized CNTs to either function as standalone materials with desirable properties or to enhance the properties of materials when integrated into composite structures.[24,26–28] Chemical interactions between CNTs and free radicals (particularly hydroxyl radicals) have been extensively studied; however, the exact underlying mechanism remains unexplored. There are two proposed mechanisms for the reaction between CNTs and free radicals. One mechanism is the formation of a radical adduct, while another process involves electron transfer during the reaction.[29] Di and trimetallic nanocomposites of ZnO, CuO and Ag_2O were studied for different potent applications, which showed better ability than the conventional materials.[30–34]

Different groups of researchers have worked on the nanocomposites of MWCNTs with metals (mono or di or trimetallic) for the biological applications.[35–37] Nazal *et al.* (2018) prepared a composite of copper, molybdenum, and nickel trioxides supported by MWCNTs for electrolytic applications in methanol oxidation reactions.[38] Noushin *et al.* (2021) synthesized Ag–CuO–ZnO@MWCNT nanocomposites by a green synthesis method. These nanocomposites were employed as heterogeneous catalysts for the preparation of substituted dihydropyrroloazepines.[39] Roodbari *et al.* (2023) reported the hydrothermal synthesis of a trioxide-based composite comprising cobalt, copper, and manganese, with rGO-MWCNTs serving as supporting materials. The composite was developed for methanol fuel cell applications.[40] Bekmezci *et al.* (2024) developed Pt-based bi- and trimetallic nanoparticles modified with MWCNTs using an arc discharge process. These materials were applied in the sensing of uric acid.[41]

After a critical review of literature, it has been found that the data on MWCNT-modified trimetal oxide nanocomposites are very limited, and most of the nanocomposites are used as sensors and catalysts for organic modifications. None of the previously reported nanocomposites were used as photocatalysts, antibacterial agents and antioxidant agents. The novelty of this research lies in reporting MWCNT-Modified Ag_2O/CuO/ZnO Nanocomposites for the first time using a sol–gel method, and the multifunctional nature of the nanocomposite as a photocatalyst, antibacterial agent and antioxidant agent is yet to be investigated.

Focusing on the high efficacy of nano hybrid materials and the wide gap in the literature, this research work was designed to synthesize ACZ-NC and MWCNTs@ACZ-NC by the sol–gel method. To study the physiochemical characteristics, EDX (mapping), SEM, FTIR spectroscopy, XRD, and DRS approaches were employed. Under solar light, in order to degrade Rh-6G, the fabricated samples were employed as photocatalysts and the effects of initial concentration, pH, catalyst concentration, and multiple uses of the catalyst were studied. Moreover, the antioxidant potential of both samples was evaluated against ABTS free radicals and the percentage activity was compared to that of ascorbic acid.

2. Materials and methods

2.1 Reagents

In this study, all the chemicals used were of analytical grade. Copper(II) nitrate pentahydrate ($Cu(NO_3)_2 \cdot 5H_2O$), zinc(II) nitrate hexahydrate ($Zn(NO_3)_2 \cdot 5H_2O$), silver(I) nitrate ($AgNO_3$), rhodamine 6G ($C_{28}H_{31}N_2O_3Cl$), sodium hydroxide (NaOH), and 2,2′-azino-bis(3-ethylbenzothiazoline-6-sulfonic acid) ($C_{18}H_{18}N_4O_6S_4$) commonly known as ABTS, and methanol (CH_3OH) were bought from Sigma-Aldrich and used without further modification. The MWCNTs were bought from Sigma-Aldrich and functionalized

with carboxylic groups. The working solution was prepared using deionized water (DIW). Glassware was washed thoroughly with DIW and then rinsed with acetone. Afterward, the dehydration of glassware, used for the synthesis of NCs, was made in an oven at 100 °C.

2.2 Synthesis of ACZ-NCs

In 10 mL of DIW, 4.55 g of $Zn(NO_3)_2 \cdot 5H_2O$, 3.15 g of $AgNO_3$, and 3.66 g of $Zn(NO_3)_2 \cdot 5H_2O$ were individually mixed under constant stirring for 30 min. Aqueous solutions of Zn, Cu, and Ag were blended with energetic stirring in a beaker and thermally treated at 60 °C for 30 min. Then, a 1 M NaOH solution was introduced to adjust the pH to 10 for 3 h, and the prepared material was constantly heated as well as stirred at 60 °C. Following a 24 h cooling period at room temperature, the mixture was clarified and given three DIW washes. After drying at 100 °C for 8 h in an electric oven, the final solid was calcined in a muffle furnace at 350 °C for 4 h.

2.3 Synthesis of MWCNTs@ACZ-NC

For the synthesis of MWCNTs@ACZ-NC, 4.55 g of $Zn(NO_3)_2 \cdot 5H_2O$, 3.15 g of $AgNO_3$, and 3.66 g of $Zn(NO_3)_2 \cdot 5H_2O$ were each dissolved separately with constant stirring for 30 min in 20 mL of DIW. The mixture that resulted by vigorously mixing these solutions in a beaker and heating at 60 °C for 30 min was marked as S1. After ultrasonic distribution in 40 mL, 0.154 g of –COOH-functionalized MWCNTs was introduced to S1. Then, 0.5 M NaOH solution was added dropwise to lower the pH down to 10. After heating to 80 °C and stirring for 5 h, the reaction mixture was allowed to age at ambient temperature for 24 h. After filtering and four rounds of rinsing with hot distilled water, the mixture was dried at 100 °C in an oven. After that, the obtained solid product was tightly sealed in a sample vial after calcination for 4 h in a muffle furnace at 350 °C.

2.4 Instrumentation

To characterize thoroughly, ACZ-NC and MWCNTs@ACZ-NC were subjected to a series of physicochemical investigations. The Debye–Scherrer equation was used to quantify the crystallite size, while XRD using a Philips X'Pert diffractometer was performed to characterize the crystalline structure. A JEOL JSM-5600LV from Tokyo (Japan) was deployed to investigate the surface morphology as well as microstructure. EDX spectroscopy was performed using an INCA-200 system from the UK to analyze the elemental composition. By using a Nicolet 560 FT-IR spectrometer, the surface functional groups between 4000 and 400 cm^{-1} were assessed. The DRS spectra were recorded using a DRS model lambda 950, and Tauc plot was used to determine the band gap energy.

2.5 Photocatalytic assay

The photocatalytic activity of all the synthesized samples, consisting of ACZ-NC, MWCNTs@ACZ-NC, and the sample without a catalyst, was assessed in the decomposition of Rh-6G dye. First, distilled water was used to prepare Rh-6G's standard solution, at a concentration of 15 ppm. Then, 20 mg of formulated samples were added to a reaction vessel containing 100 mL of this solution. For 30 min, the mixture was blended in darkness in order to achieve sorption equilibrium. A double-beam UV-vis spectrophotometer was used to systematically assess the sample after it had been exposed to simulated solar radiation for a predefined amount of time. The variations in the absorbance maxima were monitored over time.

2.6 Antibacterial assay

The antibacterial efficacy of ACZ-CS and MWCNT@ACZ-CS was evaluated against *S. aureus* and *E. coli* using the agar well diffusion protocol. Bacterial cultures were inoculated onto nutrient agar plates, and wells were bored to accommodate the test substances. The synthesized samples, *i.e.* ACZ-NC and MWCNTs@ACZ-NC, were dispersed in distilled water (1 mg in 10 mL) and poured into the wells, and the plates were incubated at 37 °C for 24 h. The diameter of the clear zone of inhibition surrounding each well was measured to determine the extent of bacterial growth inhibition. Larger zones of inhibition indicate greater antibacterial activity. Control wells containing sterile distilled water were included for comparison. The results were analyzed to compare the antibacterial efficacy of ACZ-NC and CNTs@ACZ-NC against the control groups.

2.7 Antioxidant assay

To assess the antioxidant activity, the ABTS radical cation was initially produced through mixing 5 mM potassium per sulfate with 14 mM ABTS in a 12 : 8 (w/w) and 1 : 1 (v/v) proportion in the absence of light for 16 h. The solution's absorbance was then assessed at a wavelength of 734 nm. By ultrasonically dispersing 5, 25, 50, 75, 100, 200 and 400 μg of the synthesized nanostructures in 1 mL solution for 30 min at normal temperature, stock suspensions of nanostructures were created. Then, a mixture containing 0.15 mL of $ABTS^{\bullet+}$ solution as well as 0.2 mL of produced nanostructure suspension was subjected to UV analysis after aging for 30 min. At 734 nm, the absorbance of this mixture was measured. For computing percent ABTS free radical inhibition activity, eqn (1) was used where A_i stands for sample's absorbance, while A_o refers to control's absorbance. The average of duplicate results is reported herein, and for the statistical analysis, Microsoft excel 2013 version was used where a *t*-test was applied:

$$\%\ \mathrm{RSA} = \left[\left(\frac{A_o + A_i}{A_o}\right)\right] \times 100 \quad (1)$$

3. Results and discussion

3.1 XRD analysis

Fig. 1 displays the XRD patterns of ACZ-NC as well as MWCNT-ACZ, which exhibit Bragg's reflections corresponding to Ag_2O, CuO, ZnO, and CNTs. The diffraction peak at 44.39 resulted from the diffraction of X-rays from the (111) *hkl* plane of the carbon, confirming the existence of CNTs in the sample, corresponding to JCPDS card no. 01-080-0017. The diffraction peaks for Ag_2O were observed at 17.31, 27.93, 33.59 and 38.24, resulting from the

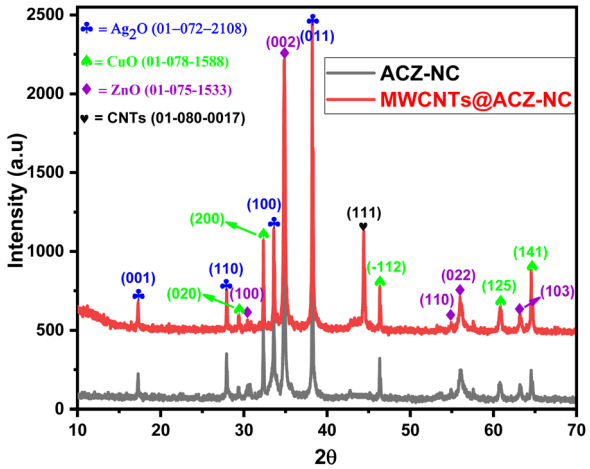

Fig. 1 XRD patterns of ACZ-NC and MWCNTs@ACZ-NC.

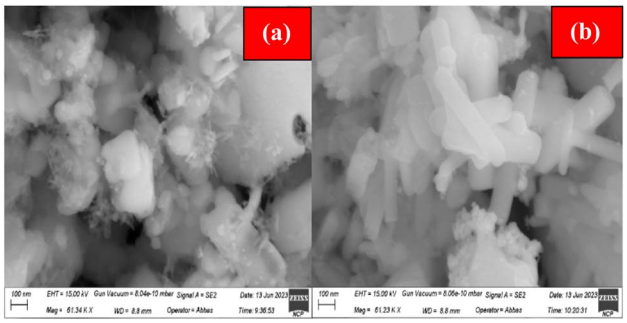

Fig. 2 SEM micrographs of ACZ-NC (a) and MWCNTs@ACZ-NC (b), showing morphological variations.

efficient overlap of X-rays diffracted from the (001), (110), (100) and (011) *hkl* planes, respectively. This confirmed the hexagonal geometry of Ag_2O, which had a lattice number of 164 and a symmetry group of $P\bar{3}m$. The lengths of two coordinates, *i.e.*, *a* and *b* were equal, each measuring 3.0720 Å, while *c* measured 4.9410 Å. Interfacial angles (α as well as β) were 90° and γ was 120°. These data matched well with that reported on JCPDS card no. 01-072-2108. It was found that Ag_2O had a particle size of 14.25 nm with crystal deformation of 0.074 percent. Diffraction peaks along the *hkl* values, *i.e.* 29.43(020), 32.35(200), 46.25(–112), 60.83(125), and 64.54(141), corresponded to JCPDS card no. 01-078-1588. These peaks confirmed the orthorhombic configuration of the CuO crystallite with space number of 38 and a space group of *Bmm*2. Three-dimensional sizes ($a = 5.3510$, $b = 6.0200$ and $c = 9.3400$) were different in length with all the interfacial angles of 90°. With a lattice strain of 0.089 percent, the crystallite size of CuO was determined to be 14.02 nm. Diffraction peaks at 2-theta positions along with the respective *hkl* planes were 30.38(100), 34.87(002), 54.93(110), 55.59(022), and 63.20(103), corresponding to a hexangular ZnO crystallite with a symmetry group of $P6_3mc$ and a space number of 186 (JCPDS card: 01-075-1538). The dimensions of two coordinates (*a* and *b*) were 3.3520, while that of the third (*c*) was equal to 5.2260 Å. Additionally, α and β were 90.00° and γ was 120°. The crystallite size of ZnO was found to be 60.3 nm, having a crystal deformation of 0.192 percent.

3.2 SEM analysis

The structural analysis of ACZ-NC and MWCNTs@ACZ-NC was performed, and Fig. 2(a) and (b) demonstrates the obtained FESEM micrographs. The SEM image (Fig. 2(a)) depicts the morphological variations of ACZ-NC, where both the shape and the size of particles were non-uniform. Both individual particles and larger aggregates were clearly seen in the image; the individual particles exhibited spherical, nearly spherical, slightly elongated fiber-like structures, and polyhedral morphologies. All these particles were non-uniform that led to the formation of several defects in the sample. Cavity formation might also be due to the evaporation of solvents and the removal of volatile by-products during the drying process. These cavities were probably a result of gas release or phase separation during the gelation and drying stages. Some individual granules were also observed on the surface of larger aggregates. Individual particles in the sample had wide size distribution ranging between 15 nm and 110 nm, whereas the size of the larger aggregates was over 160 nm. Fig. 2(b) illustrates the SEM image of MWCNTs@ACZ-NC, where changes were observed in the morphology of ACZ-NC due to the incorporation of MWCNTs in their structure. MWCNTs, long cylindrical carbon structures with unique properties, significantly influence the morphology of the resulting composite. The presence of MWCNTs introduced a distinct elongated morphology as tube-like structures were apparent. Upon close observation, the ACZ-NC particles were visible on the surface of elongated tube-like structures; however, their distribution was not uniform. The number of cavities got reduced as MWCNTs filled in voids present in the original nanocomposite. The elongated tube-like structures were regularly distributed and their surfaces appeared smooth and non-porous, possibly due to the synthetic sol–gel method, which produces materials with smooth and non-porous surfaces through uniform deposition and controlled particle growth.

3.3 EDX analysis

Fig. 3((a) as well as (b)) displays the EDX mapping results of ACZ-NC and MWCNT-ACZ, which confirmed the presence of carbon from the CNTs and the metallic components, including silver (Ag), copper (Cu), zinc (Zn), and oxygen (O), corresponding to the Ag_2O, CuO, and ZnO phases. No significant impurities were detected, indicating the high purity of the synthesized nanocomposite. The elemental mapping showed that silver (Ag), copper (Cu), zinc (Zn), and oxygen (O) were uniformly distributed across the CNT matrix, indicating a well-integrated nanocomposite structure. This homogeneous distribution suggested good interaction between CNTs and MO-NPs. No significant areas of agglomeration were observed, highlighting the efficiency of the synthesis method in achieving a well-dispersed nanocomposite. The uniform distribution of elements observed in the EDX mapping aligned well with the XRD results, confirming the formation of distinct Ag_2O, CuO, and ZnO phases. The lack of significant agglomeration was further supported by the SEM images, which showed uniformly dispersed nanoparticles.

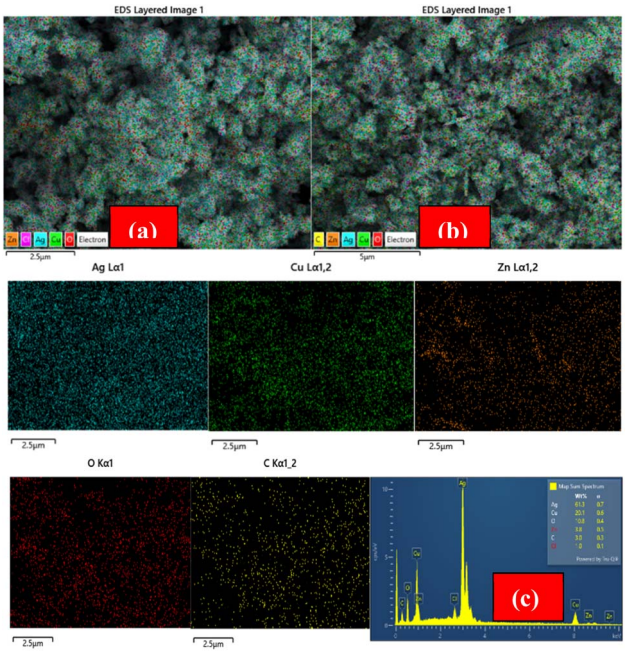

Fig. 3 EDX mapping of ACZ-NC (a) and MWCNTs@ACZ-NC. (b) EDX spectrum of MWCNTs (c).

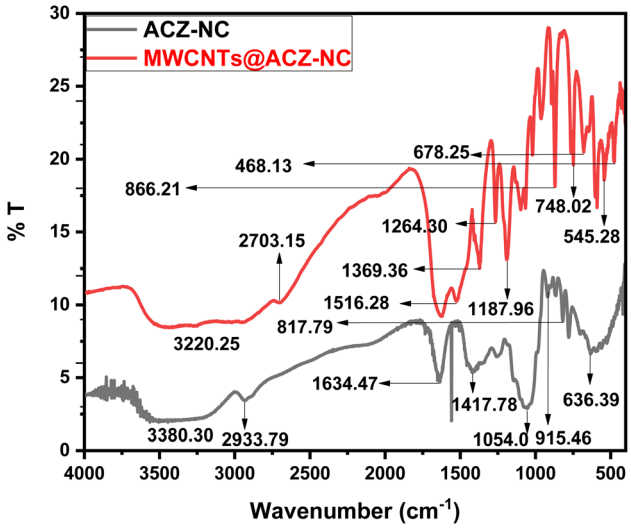

Fig. 4 FT-IR spectra of ACZ-NC and MWCNTs@ACZ-NC, showing different vibration bands.

The EDX spectra of MWCNT@ACZ-NC displayed in Fig. 3(c) show that the peak at 0.5 keV indicates oxygen's inclusion in samples, most likely related oxides of Ag, Zn, as well as Cu. The EDX spectra of MWCNT@ACZ-NC displayed in Fig. 3(c) show that the peak at 0.5 keV indicates oxygen's inclusion in samples, most likely related oxides of Ag, Zn, as well as Cu. Ag's peaks became visible at 3.08 keV, for Cu at 0.9 and 8.05 keV, and for Zn at 1.05, 8.7, and 9.6 keV, validating samples' intended elemental composition. Additionally, a peak at 2.62 keV indicated Cl's existence. A peak for C centered at 0.21 keV corresponded to the Kα peak of carbon in EDX analysis. This peak confirmed the incorporation of MWCNTs into the nanocomposite. This peak emerged due to the characteristic X-ray emission of carbon atoms when they were excited by the incident electron beam.

3.4 FT-IR analysis

In Fig. 4, the FT-IR spectra display peaks at distinct wavenumbers (cm^{-1}), indicating points where IR radiation transfer occurred. OH absorption as well as H–O–H's stretching collision were identified as causes of two broad bands with centers at 3380.30 and 3220.25 cm^{-1}.[42] The band at 2933.79 cm^{-1} was ascribed to the C–H stretching modes of MWCNTs.[43] A slight band resulting from the C–H stretching vibration was noticed at 2703.15 cm^{-1}.[44] A notably intense band detected at 1634.47 cm^{-1} was associated with H–O–H coordinated H_2O molecule's in-plane bending.[45] A faint band at 1516.28 cm^{-1} was designated to MWCNTs' C=C expanding mode.[46] Another mild band at 1417.78 cm^{-1} was accredited to the M–OH vibrations.[47] Owing to the out-of-plane O–H bending vibrations, a fairly sharp band at 1369.36 cm^{-1} was identified.[46] A second band was detected at 1264.30 cm^{-1}, and it was determined to be a C–O stretching bond.[48] C–H in flexural vibration created a band at 1187.96 cm^{-1}.[49] The M–OH (Ag, Cu, or Zn) vibrations were assigned to the band at 1054.10 cm^{-1}.[50] The O–M–O vibrations of Ag, Cu, and Zn were recognized as band's source at 915.46 cm^{-1}.[51] M–O–M (Ag, Cu, or Zn) vibrations were represented by the band at 866.21 cm^{-1}.[52] A band at 817.79 cm^{-1} was influenced by M–O–M vibrations.[53] The C–O–M bond was the prime cause of band at 748.02 cm^{-1}.[54] The Cu–O elongation mode caused the appearance of band at 678.25 cm^{-1}.[55] The AgO bending vibrations gave rise to the band at 636.39 cm^{-1}.[56] The band at 545.28 cm^{-1} was produced by ZnO bending vibrations.[57] However, ZnO stretching vibrations caused the band at 468.13 cm^{-1}.[58] The incorporation of MWCNTs into the Ag_2O/CuO/ZnO nanocomposite significantly altered its FT-IR spectra by introducing new bands, shifting existing bands, changing intensities, broadening bands, causing the disappearance of minor bands, and potentially forming new functional groups. The introduction of MWCNTs led to the appearance of new absorption bands. These bands were attributed to the vibrational modes of the carbon nanotubes, such as C=C elongation and C–H flexing. The incorporation of MWCNTs caused shifts in the existing absorption bands of the Ag_2O/CuO/ZnO nanocomposite. This happened due to interactions between the MWCNTs and the metal oxides, which altered the local electronic environment and, consequently, the vibrational frequencies. The intensity of certain absorption bands changed. For example, the peaks corresponding to metal–oxygen stretching vibrations (*e.g.*, Zn–O, Cu–O, and Ag–O) experienced changes in their intensities due to the physical or chemical interactions with the MWCNTs. Enhanced dispersion and improved interfacial bonding led to more prominent bands or changes in the relative intensities. Moreover, the incorporation of MWCNTs enhanced the polarizability of composites due to the presence of π-electrons in carbon nanotubes. This increased polarizability also led to stronger interactions with the infrared radiation, resulting in enhanced peak intensities in the FT-IR spectra. Some minor bands either disappeared or

became less noticeable in the FT-IR spectra as they were overshadowed by the more prominent absorption features of the MWCNTs or due to changes in the vibrational modes of the composite. The incorporation of MWCNTs also induced structural changes in the nanocomposite, such as changes in crystallinity or the formation of new phases which also made some peaks more prominent in the FT-IR spectra.

3.5 DRS analysis

The optical characteristics of ACZ-NC as well as MWCNTs@ACZ-NC were investigated using DRS, and Fig. 5(a)–(c) displays the obtained findings. For both samples, absorbance edges appeared at 720.56 nm and 765.70 nm, respectively. The results depicted that both samples exhibited peak absorption in the visible spectrum. Moreover, a redshift was observed in the absorbance edge with the incorporation of CNTs, indicating that the sample absorbed more visible light, extending to a broader spectrum. Band gap energies for both samples were measured using Tauc's plots derived from the respective equations, *i.e.* eqn (2) and (3) for direct and indirect transitions. The determined energy gaps are given in Fig. 5(b) and (c), showing a slight decrease in the band gap energies, which indicated that the electronic structure of ACZ-NC was altered by the incorporation of MWCNTs. The decrease in band gap energies might be due to the interaction between the electronic structure and conductive π-electron networks of the MWCNTs.

$$\alpha h\nu = A(h\nu - E_g)^2 \quad (2)$$

$$\alpha h\nu = A(h\nu - E_g)^{1/2} \quad (3)$$

3.6 Photocatalytic activity

The photocatalytic efficacy of ACZ-NC as well as MWCNTs@ACZ-NC, synthesized through a modified sol–gel method, was assessed using Rh-6G dye as the test substrate. The Rh-6G dye was also degraded without any catalyst in order to assess its self-photolytic capability. The assessment was conducted in an outdoor setting from 11 a.m. to 3 p.m. under solar light radiation between June 3 and June 14, 2024. Light brown color's progressive decline over time indicated reaction mixture's discoloration. At 526 nm, a sharp initial decline in absorbance maxima was observed following UV-visible measurement using a double-beam spectrophotometer, which suggested that at that specific wavelength, the chromophore that caused light absorption had degraded.

This decrease was pronounced in samples containing catalysts, while it was negligible in the sample without any catalyst. The decay curve shown in Fig. 6 demonstrates a progressive decline in peak absorbance over time. A prominent as well as rapid reduction in maximum absorption occurred during initial 10 min, particularly in the MWCNT-modified sample. However, it was minimal in the sample without any catalyst. Afterward, the reduction rate slowed down in all samples. The sample modified with MWCNTs exhibited the greatest reduction in absorbance maximum.

Rh-6G's percentage degradation was determined using eqn (4). Fig. 7 illustrates the results for all samples where the sample containing ACZ-NC showed a degradation of 97.31%, while the MWCNTs@ACZ-NC exhibited 99.61% degradation of Rh-6G. In contrast, the sample without a catalyst showed only 3.52% degradation. These results emphasized the relative performance of each sample to decompose Rh-6G under specified research conditions. The findings showed that among all samples, the MWCNTs@ACZ-NC exhibited the highest photocatalytic efficiency, whereas the sample without any catalyst showed poor catalytic activity.

$$\%\ \text{Degradation} = C_o - C_e/C_o \times 100 \quad (4)$$

The degradation rate constants determined using eqn (5) for photocatalytic reactions conducted with ACZ-NC, MWCNTs@ACZ-NC, and without a catalyst were 0.05368,

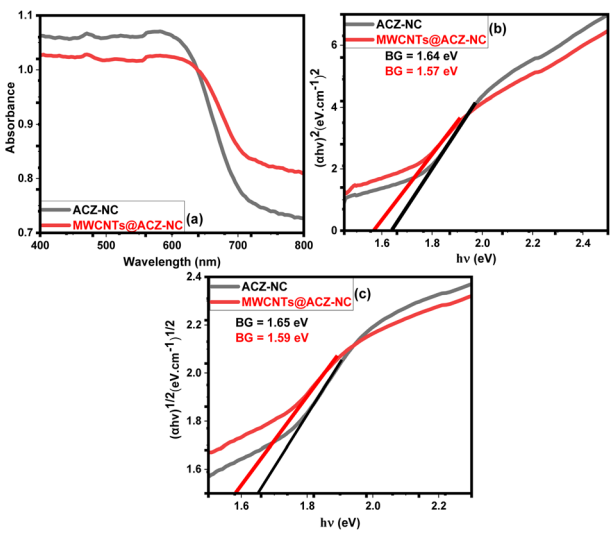

Fig. 5 DRS spectrum (a), direct band gap (b) and indirect band gap (c) of ACZ-NC and MWCNTs@ACZ-NC.

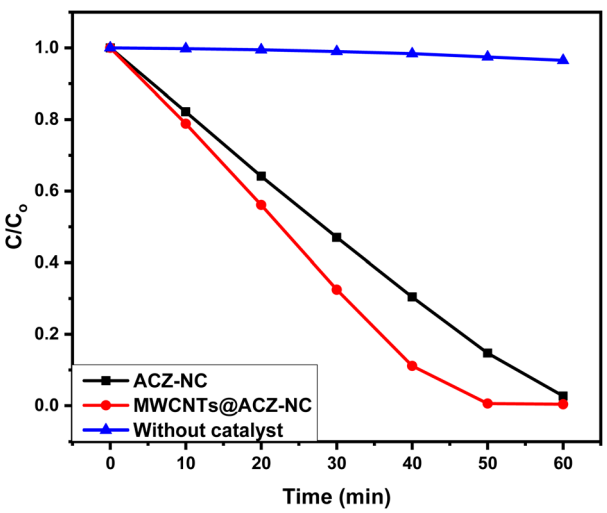

Fig. 6 Degradation profile of Rh-6G in the presence of solar light and the synthesized nanocomposites.

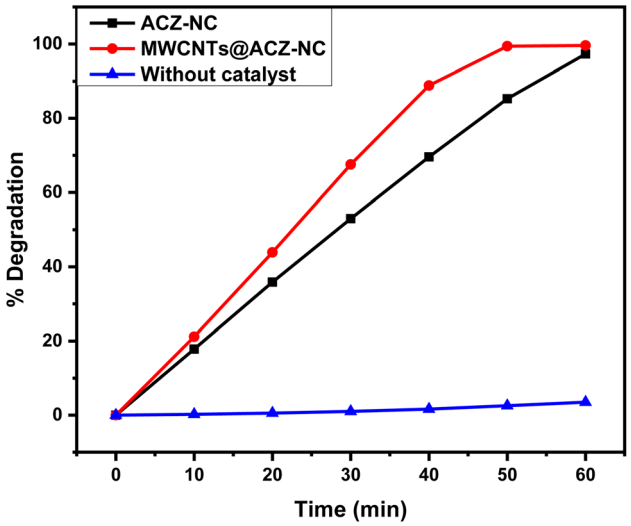

Fig. 7 Percentage degradation of Rh-6G in the presence of solar light and the synthesized nanocomposites.

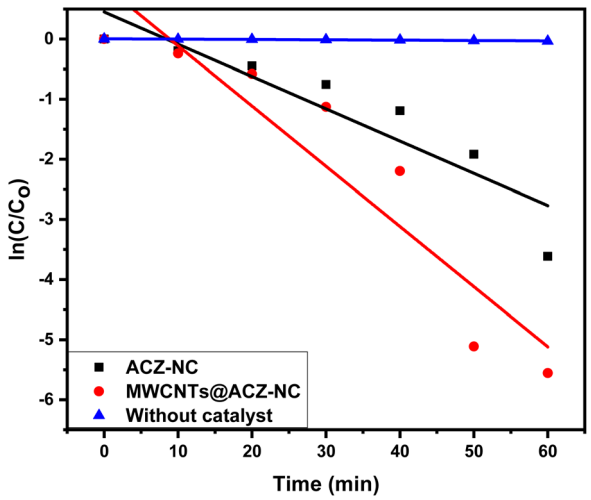

Fig. 8 Degradation rate constant of the photocatalytic reaction carried out in the presence of synthesized nanocomposites.

0.10012, and 5.90528 per min, respectively (Fig. 8). These figures simplify Rh-6G breakdown in a specified environment by providing insights into the photocatalytic activity ratio of each sample. A higher rate constant signifies enhanced decomposition rate, implying enhanced photocatalytic activity in fabricated samples. The outcomes indicated that MWCNTs@ACZ-NC showed the fastest rate constant, *i.e.*, 0.10012 per min, among the examined samples. This suggested that MWCNT@ACZ-NC could potentially be more efficient at promoting the target compound's breakdown.

$$\ln(C/C_t) = -kt \quad (5)$$

3.7 Factors affecting the photocatalytic reaction

3.7.1 Effect of pH on % degradation. First, 0.1 M NaOH as well as 0.1 M HCl were used to alter the Rh-6G solution's pH. By changing the solution's pH, the proportion of H^+ and OH^- was influenced, which was accountable for the generation of free radicals responsible for the breakdown of Rh-6G dye.[59,60] The impacts of pH modifications on the % degradation rate were carefully monitored (Fig. 9). Research revealed the degradation of 68.38% at pH 4, 72.59% at pH 5, 76.91% at pH 6, 81.1% at pH 7, 85.334% at pH 8, 89.4% at pH 9, 93.74% at pH 10, 97.21% at pH 11, 99.61% at pH 12, and 96.76% at pH 13. The data indicated that the degradation rate increased with the progression of pH. The ionic ($Rh\text{-}6G^+$) and non-ionic (Rh-6G) nature represent that Rh-6G has a binary existence with the latter responsible for its increasing reactivity in a basic environment, indicating that this form significantly influences its degradation. In an alkaline medium, this form allows greater dye accessibility during cavity contraction, where extreme cavitation accelerates decomposition. Additionally, it has been found that dye's hydrophilic nature under alkaline conditions favors greater degradation compared to that under acidic conditions.[61] Moreover, assumption can be made that hydroxyl radical assault, that is generally more favorable at higher pH levels, is what is driving the primary chemical reaction in this case. In addition, the lower degradation rate of Rh-6G at a high pH of 13, compared to the optimal pH, was due to the rapid scavenging of hydroxyl radicals at very high pH levels. This rapid scavenging reduced the availability of hydroxyl radicals for specific oxidation of Rh-6G dye.[62]

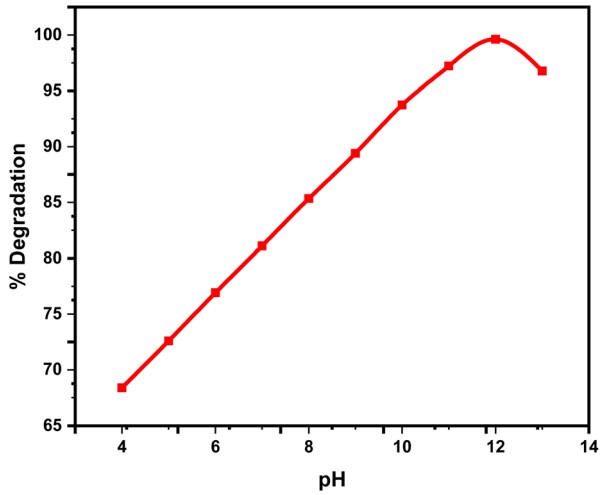

Fig. 9 Effect of pH on the photocatalytic activity.

3.7.2 Effect of dose on % degradation. Fig. 10 illustrates the decomposition of Rh-6G using different concentrations (10, 15, 20, 25, and 30 mg) of catalysts. The findings revealed that the percentage of degradation increased proportionately with the increase in catalyst dose. The dye's degradation rate increased with the increase in catalyst concentration.[63] A catalyst dose of 20 mg was found to have the maximum activity, suggesting this as an optimal photocatalyst dosage for a MWCNT-modified Ag_2O/CuO/ZnO NC photocatalytic process. The number of binding sites which interact with the dye increased as NC's total surfaced area increased at higher doses. When MWCNTS@ACZ-NC's concentration increased from 10 to 20 mg, Rh-6G's %

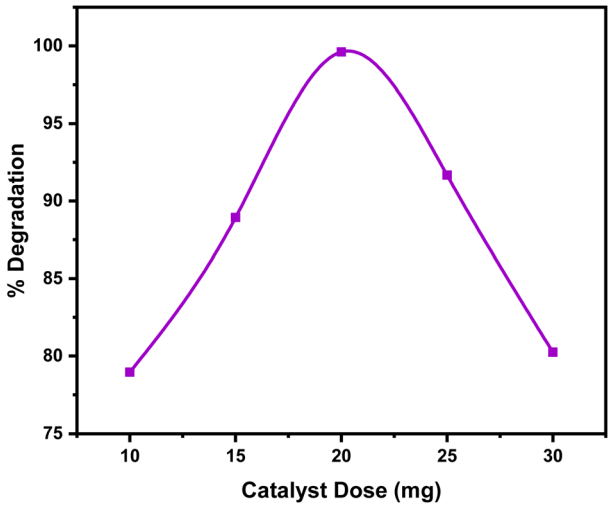

Fig. 10 Effect of catalyst dose (mg) on the photocatalytic activity.

decomposition enhanced from 78.96% to 99.61%. However, degradation slightly decreased to 91.67% at 25 mg, which further declined to 80.25% at 30 mg. NC's expanded surface area, which resulted in more active sites interacting with the dye, was thought to be the cause of this increase in degradation with higher catalyst doses.[64] As the active site density on NCs increased, highly reactive species were produced, improving degradation. However, at larger doses of 25 and 30 mg, reduced dye degradation suggested the fabrication of intermediate by-products. Additionally, at greater quantities, the accumulation of the NCs can occur, possibly causing reduced degradation. Less photon contact with the catalyst surface along with less effective light absorption by the catalyst could also be the reason of this drop.[65]

3.7.3 Effect of initial concentration on % degradation. Rh-6G's light-induced decomposition had been investigated using different starting concentrations (5, 10, 15, 20, and 25 ppm), yielding % degradation rates of 72.97, 89.26, 99.61, 92.79, and 83.05, respectively (Fig. 11). Once the starting concentrations reached 15 ppm, there was a noticeable increase in dye degradation. However, further increases in solution strength led to a reduction in degradation percentage. An initial concentration of 15 ppm was identified to be a favorable condition for upgraded photocatalytic performance, as evidenced by the maximum degradation efficiency of 99.61%.

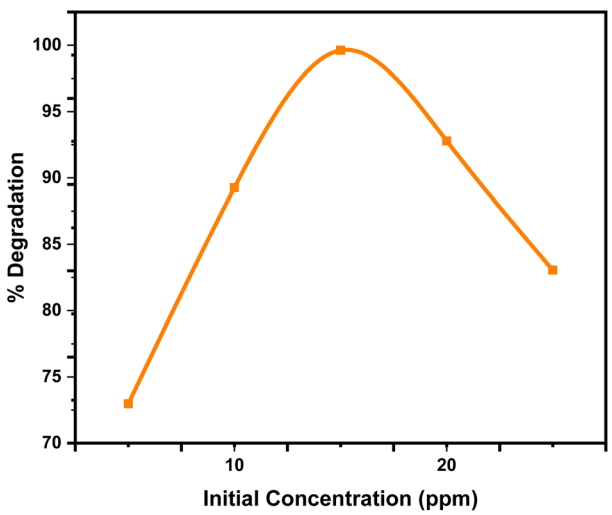

Fig. 11 Effect of initial concentration (ppm) on the photocatalytic activity.

At elevated amounts, the reactive centers of MWCNTs@ACZ-NC became fully occupied and saturated, resulting in reduced degradation. The reduced hydroxyl ion production and, as a result, reduced photocatalytic efficiency can result from the elevated concentrations interfering with light interaction on the catalyst surface. Additionally, the formation of breakdown products that compete with Rh-6G for restricted catalytic sites on the NC surface, along with reactive intermediates formation, could contribute to this decline.

3.7.4 Effect of recycling on % degradation. MWCNTs@ACZ-NC catalyst's durability during extended exposure as a photocatalyst is an important consideration. To assess its stability, it underwent five consecutive reuse cycles; the corresponding % degradation for cycles 1 to 5 was 99.61, 98.21, 93.74, 87.65, and 81.96 respectively (Fig. 12). The catalyst's pristine state, which provided an ideal abundance of active sites, was probably the cause of the high initial degradation efficiency (99.61%). A gradual decrease in efficiency may be attributed to early catalyst deactivation, minor structural alterations, or surface impurities. Due to the loss of catalytic activity and dye adsorbed on the photocatalyst during the recycling process, the deactivation rate may deal with a moderate decrease.[66] Furthermore, impurities from reaction environment may collect on the catalyst surface during reuse, leading to decreased catalytic efficiency. The loss of active molecules, agglomeration, and structural modifications are some of the factors that might deactivate a catalyst across several phases, reducing the number of active sites that are available for light-induced reactions.

3.8 Antibacterial activity

The antibacterial activity of the ACZ-NC and MWCNTs against the selected bacterial strain was determined by an agar well diffusion method, and the obtained results are shown in Fig. 13. The data show (Table 1) that the activity of the sample increases with the increase in the concentration of the samples. The

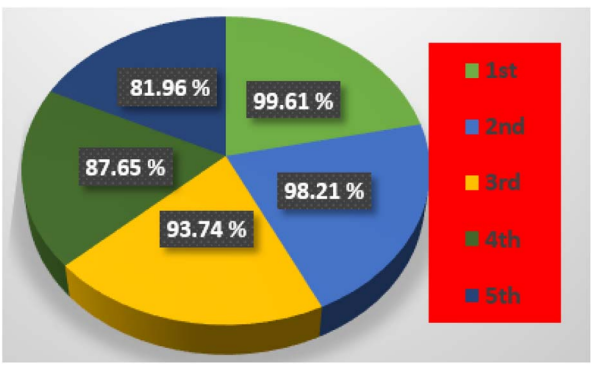

Fig. 12 Recycling efficiency of the MWCNTs@ACZ-NC.

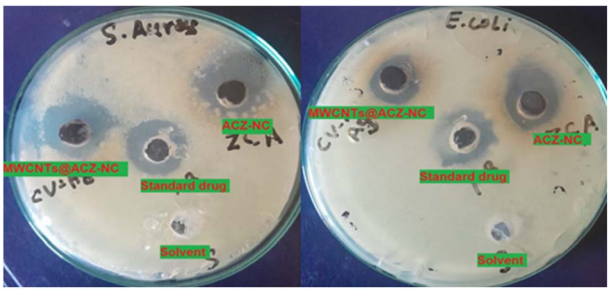

Fig. 13 Antibacterial activity of the synthesized nanocomposites.

Table 1 Antibacterial activity results of ACZ and MWCNTs@ACZ-NC

	Samples			
Bacterial species	ACZ-NC	MWCNTs@ACZ-NC	Standard drug	Solvent
S. aureus	22.5	20	19.5	00
E. coli	18.3	1.6	19	00

enhanced activity at a higher concentration is due to the large number of particles that interact with the bacterial surface. It is also been observed that the activity of the ACZ-NC is higher than that of the MWCNTs@ACZ-NC, which might be due to the incorporation of CNTs that occupy/cover binding sites responsible for direct interaction with the bacterial cell, which led to a weak interaction between the bacterial surface and the ACZ-NC. The incorporation of CNTs also altered the surface morphology, surface charge and chemical functionality of the ACZ-NC, which made the surface less compatible with the bacterial outer membrane and this reduced interaction led to a lower antibacterial efficacy of the MWCNTs@ACZ-NC. Moreover, the incorporation of MWCNTs led to an increase in particle size, as observed in the SEM analysis. This increase in size may hinder the ability of the particles to effectively penetrate bacterial cells.

3.9 Antioxidant activity

By testing against the $ABTS^{\bullet+}$ solution and compared to that of ascorbic acid as a control, the antioxidant activities of ACZ-NC as well as MWCNTs@ACZ-NC were evaluated, with the findings presented in Table 2. To evaluate the percentage radical scavenging activity, ascorbic acid and the synthesized samples were exposed to a solution containing $ABTS^{\bullet+}$ at different doses of 5, 25, 50, 100, 200 and 400 μg mL^{-1}. The antioxidant activity rose as the concentration of both samples increased, suggesting that to neutralize the $ABTS^{\bullet+}$ radical cation, a greater amount of antioxidants were needed.[67,68] With the increase in concentration, the percentage radical scavenging activity increased. ACZ-NC displayed scavenging activity spanning from 26.076% to 91.336% at different concentrations while the scavenging activity of MWCNTs@ACZ-NC ranged from 27.144% to 95.924%. The antioxidant capacity of both NCs may be explained by the negatively charged NCs' electron-donating surface, which may be in charge of containing the ABTS free radical species.[68,69] As it was able to combine more reactive oxygen species, the antioxidant activity was stronger.[70] ABTS free radical searching activity was observed to increase when the NP portion was increased, that may be attributed to an increased number of NPs that could engage with ABTS free radicals.[71] The antioxidant concentration at which fifty percent of $ABTS^{\bullet+}$ radical cation can be neutralized is known as the IC_{50} value. The IC_{50} value for ACZ-NC was calculated to be 80.65 μg mL^{-1}. For MWCNTs@ACZ-NC, the IC_{50} value was 59.22 μg mL^{-1}, while 49.79 μg mL^{-1} was the IC_{50} value of vitamin C. This indicates that MWCNTs@ACZ-NC exhibited a greater activity than that of the unmodified ACZ-NC, but was less active than that of ascorbic acid. Standard deviation indicates the spread of antioxidant activity values around the mean and helps assess

Table 2 Antioxidant activity of ACZ-NC and MWCNTs@ACZ-NC against the ABTS free radicals

Samples	Concentration (μg mL^{-1})	% RSA	IC_{50} (μg mL^{-1})	Variance (S^2)	Standard deviation (S)	Correlation between dose and % RSA
ACZ-NC	5	26.076	80.65	2.65	1.63	0.110
	25	34.188				
	50	48.228				
	100	65.916				
	200	81.004				
	400	91.336				
MWCNTs@ACZ-NC	5	27.144	59.22	2.71	1.64	0.119
	25	36.432				
	50	53.796				
	100	71.124				
	200	84.612				
	400	95.924				
Ascorbic acid	5	21.92	92.74	3.09	1.75	0.102
	25	33.58				
	50	47.956				
	100	57.396				
	200	83.976				
	400	94.068				

consistency. A smaller standard deviation suggests high precision and consistency in the results. A larger standard deviation indicates greater variability, suggesting less consistency in the antioxidant activity measurements. The values were found to be 1.63, 1.64, and 1.75 for ACZ-NC, MWCNTs@ACZ-NC, and ascorbic acid, respectively, indicating that ACZ-NC demonstrated the highest precision and consistency in its results. The variance, which is square of the standard deviation, represents the mean square error from the mean and measures the spread of antioxidant activity values. Higher variance suggests greater differences in antioxidant activity between samples or experimental conditions. The variance values were 2.65, 2.71, and 3.09 for ACZ-NC, MWCNTs@ACZ-NC, and ascorbic acid, respectively. These results indicated that ACZ-NC exhibited the least variation in antioxidant activity across samples or conditions. The correlation between dose and % RSA was determined to be 0.110, 0.119, and 0.102 for ACZ-NC, MWCNTs@ACZ-NC, and ascorbic acid, respectively. This suggested that ascorbic acid showed the strongest relationship, where higher doses were not associated with increased % RSA, while higher doses of MWCNTs@ACZ-NC were linked to increased % RSA. ACZ-NC leveraged electron donation, redox cycling, SPR effects, and metal–ligand coordination to neutralize free radicals and reduce oxidative stress while addition of MWCNTs enhanced electron transfer, increased active sites, and stabilized reactive species, making the composite more effective in antioxidant applications.

4. Conclusions

In this study, ACZ-NC and MWCNTs@ACZ-NC were prepared by the sol–gel method, which allows for better control over size and morphology, leading to the synthesis of uniform samples, as evident from the EDS mapping results. This method is more efficient, faster, and simpler than the traditional approaches, making it a superior strategy for preparing these nanocomposites. The physicochemical analysis revealed that the crystallinity and particle size were significantly affected by the interaction between MWCNTs and the trimetal oxide NC. A slight decrease in the band gap energy of MWCNTs@ACZ-NC was also observed. The incorporation of MWCNTs enhanced the photocatalytic efficiency of the nanocomposite due to increased conductivity and improved electron–hole separation. The optimization process indicated that the pH, catalyst dose, and the initial concentration of Rh-6G significantly influenced the photocatalytic process. A similar improvement was observed in the antioxidant activity of MWCNTs@ACZ-NC, attributed to the increased number of binding sites and enhanced electron transfer, which stabilized free radicals. However, a slight decrease in the antibacterial potential of MWCNTs@ACZ-NC was noted, possibly due to the increase in particle size, which may have hindered the penetration of the material into bacterial cells.

Data availability

All relevant experimental details and raw data, including characterization results (XRD, SEM, FTIR, DRS and EDX mapping) and measurements of photocatalytic, antibacterial, and antioxidant activity, have been archived and are available upon request. Due to the large volume of data associated with the calculation results in this study and the limitations of our institution's data-sharing policy, it is not feasible to upload all the data to public networks. However, we have disclosed the relevant calculation script files involved in the research process. The data supporting the findings of this study are available from the corresponding author upon reasonable request. Any additional information regarding the materials and methods used in this study can also be provided upon request to support further inquiries and reproducibility of the results.

Author contributions

Amjad Latif Lone – formal analysis and writing – original draft; Sadiq Ur Rehman – supervision, project administration; Sirajul Haq, Nadia Shahzad and Muhammad Imran Shahzad – conceptualization, methodology and project administration; Shafia Shujaat – visualization, and writing – original draft; Mohammad Khalid Al-Sadoon – software, data curation and funding acquisition; Jamoliddin Razzokov and Abdus Samad – validation and writing – review & editing.

Conflicts of interest

There are no conflicts to declare.

Acknowledgements

The authors would like to extend their sincere appreciation to the Researchers Supporting Project Number (RSP2025R410), King Saud University, Riyadh, Saudi Arabia.

References

1 S. Haq, W. Rehman and M. Waseem, *J. Inorg. Organomet. Polym. Mater.*, 2018, **29**, 651–658.
2 S. Haq, W. Rehman and M. Rehman, *J. Inorg. Organomet. Polym. Mater.*, 2020, **30**, 1197–1205.
3 V. Lobo, A. Patil, A. Phatak and N. Chandra, *Pharmacogn. Rev.*, 2010, **4**, 118–126.
4 P. Gupta, S. P. Authimoolam, J. Z. Hilt and T. D. Dziubla, *Acta Biomater.*, 2015, **27**, 194–204.
5 J. Lee, N. Koo and D. B. Min, *Compr. Rev. Food Sci. Food Saf.*, 2004, **3**, 21–33.
6 J. A. Klein and S. L. Ackerman, *J. Clin. Invest.*, 2003, **111**, 785–793.
7 D. Malakar, H. N. Malik, D. Kumar, S. Saini, V. Sharma, S. Fatima, K. K. Bajwa and S. Kumar, *Advances in Animal Genomics*, 2020, vol. 4, pp. 33–48.
8 G. Waris and H. Ahsan, *J. Carcinog.*, 2006, **5**, 1–8.
9 V. Herynek, P. Matou, M. Moskvin, V. Hunto, M. Slouf and D. Hor, *Colloids Surf., B*, 2021, 111824, DOI: **10.1016/j.colsurfb.2021.111824**.
10 M. B. Kulkarni and S. Goel, *Energy Policy*, 2006, **34**(5), 1984–1991.

11 N. Verma and N. Kumar, *ACS Biomater. Sci. Eng.*, 2019, **5**, 1170–1188.
12 F. Ijaz, S. Shahid, S. A. Khan, W. Ahmad and S. Zaman, *Trop. J. Pharm. Res.*, 2017, **16**, 743–753.
13 J. Aien, A. A. Khan, S. Haq, A. R. Khan, K. Elmnasri, M. Ben Ali, M. S. AL-Harbi, M. I. Alghonaim, S. A. Alsalamah, A. A. Qurtam, F. Boufahja, A. Hedfi and M. Dellali, *Crystals*, 2023, 330, DOI: **10.3390/cryst13020330**.
14 S. Ghazal, N. Khandannasab, H. Ali, Z. Sabouri, A. Rangrazi and M. Darroudi, *Ceram. Int.*, 2021, **47**, 27165–27176.
15 M. Shahzad Shirazi, M. Moridi Farimani, A. Foroumadi, K. Ghanemi, M. Benaglia and P. Makvandi, *Sci. Rep.*, 2022, **12**, 1–15.
16 H. Yousaf, A. Mehmood, K. S. Ahmad and M. Raffi, *Mater. Sci. Eng., C*, 2020, **112**, 110901.
17 A. U. Khan, A. U. Khan, B. Li, M. H. Mahnashi, B. A. Alyami, Y. S. Alqahtani, K. Tahir, S. Khan and S. Nazir, *Photodiagn. Photodyn. Ther.*, 2020, 101814, DOI: **10.1016/j.pdpdt.2020.101814**.
18 G. Maheshwaran, A. Nivedhitha Bharathi, M. Malai Selvi, M. Krishna Kumar, R. Mohan Kumar and S. Sudhahar, *J. Environ. Chem. Eng.*, 2020, **8**, 104137.
19 S. B. Ghaffari, M. H. Sarrafzadeh, Z. Fakhroueian and M. R. Khorramizadeh, *Mater. Sci. Eng., C*, 2019, **103**, 109827.
20 E. Albiter, A. S. Merlano, E. Rojas, J. M. Barrera-andrade, Á. Salazar and M. A. Valenzuela, *J. Compos. Sci.*, 2021, **5**(1), 1–40.
21 R. Vinayagam, R. Selvaraj, P. Arivalagan and T. Varadavenkatesan, *J. Photochem. Photobiol., B*, 2020, **203**, 111760.
22 T. A. Singh, A. Sharma, N. Tejwan, N. Ghosh, J. Das and P. C. Sil, *Adv. Colloid Interface Sci.*, 2021, **295**, 102495.
23 J. Vera, W. Herrera, E. Hermosilla, M. Díaz, J. Parada, A. B. Seabra, G. Tortella, H. Pesenti, G. Ciudad and O. Rubilar, *Antioxidants*, 2023, 784, DOI: **10.3390/antiox12040784**.
24 J. Zhang, H. Zhang, S. Wang and M. Liu, *Polym. Degrad. Stab.*, 2017, **144**, 93–99.
25 G. Cirillo, S. Hampel, R. Klingeler, F. Puoci, F. Iemma, M. Curcio, O. I. Parisi, U. G. Spizzirri, N. Picci, A. Leonhardt, M. Ritschel and B. Büchner, *J. Pharm. Pharmacol.*, 2011, **63**, 179–188.
26 R. M. Lucente-Schultz, V. C. Moore, A. D. Leonard, B. K. Price, D. V. Kosynkin, M. Lu, R. Partha, J. L. Conyers and J. M. Tour, *J. Am. Chem. Soc.*, 2009, **131**, 3934–3941.
27 K. Rajavel, R. Gomathi, S. Manian and R. T. Rajendra Kumar, *J. Taibah Univ. Med. Sci.*, 2016, **11**, 469–477.
28 X. Shi, B. Jiang, J. Wang and Y. Yang, *Carbon*, 2012, **50**, 1005–1013.
29 X. Xu, Y. You, X. Liu, D. Wei, Y. Guan and A. Zheng, *Carbon*, 2021, **177**, 189–198.
30 R. S. Shinde, R. A. More, V. A. Adole, P. B. Koli, T. B. Pawar, B. S. Jagdale, B. S. Desale and Y. P. Sarnikar, *Curr. Res. Green Sustainable Chem.*, 2021, **4**, 100138.
31 M. Barwant, Y. Ugale, S. Ghotekar, P. Basnet, S. Pansambal, A. Murthy, T.-D. Pham, M. Bilal, R. Oza and V. Karande, Plant-Mediated Biological Synthesis of Ag-Ago-Ag2O Nanocomposites Using Leaf Extracts of Solanum Elaeagnifolium for Antioxidant, Anticancer, and DNA Cleavage Activities, *Research Square*, 2021, preprint, DOI: **10.21203/rs.3.rs-973781/v1**.
32 F. Ur Rehman, R. Mahmood, M. Ben Ali, A. Hedfi, M. Almalki, A. Mezni, W. Rehman, S. Haq and H. Afsar, *Materials*, 2021, **14**, 1–13.
33 E. El-Mohsnawy, A. El-Shaer, F. El-Gharabawy, E. E. El-Hawary and A. E. R. R. El-Shanshoury, *Braz. J. Microbiol.*, 2023, **54**, 2807–2815.
34 S. Hameed, A. T. Khalil, M. Ali, M. Numan, S. Khamlich, Z. K. Shinwari and M. Maaza, *Nanomedicine*, 2019, **14**, 655–673.
35 J. Zhang, H. Zhang, S. Wang and M. Liu, *Polym. Degrad. Stab.*, 2017, **144**, 93–99.
36 G. Cirillo, S. Hampel, R. Klingeler, O. Ilaria, U. Gianfranco and N. Picci, *JPP*, 2011, 179–188.
37 D. M. Stanković, M. Ognjanović, M. Fabián, V. V. Avdin, D. D. Manojlović, S. V. Đurić and B. B. Petković, *Surf. Interfaces*, 2021, **25**, 101211.
38 M. K. Nazal, O. S. Olakunle, A. Al-Ahmed, B. Merzougui, A. Abualkibash, A. Sultan, A. Bin Yousaf and S. J. Zaidi, *J. Electroanal. Chem.*, 2018, **823**, 98–105.
39 A. Noushin, A. Varasteh-Moradi, S. Z. Sayyed-Alangi and Z. Hossaini, *Appl. Organomet. Chem.*, 2021, **35**, e6295.
40 N. Jamshidi Roodbari, S. R. Hosseini and A. Omrani, *Energy Fuels*, 2023, **37**, 5489–5498.
41 M. Bekmezci, N. Y. Ertas, M. Akin, I. Isik and F. Sen, *Next Res.*, 2024, 100081.
42 S. A. Moon, B. K. Salunke, B. Alkotaini, E. Sathiyamoorthi and B. S. Kim, *IET Nanobiotechnol.*, 2015, **9**, 220–225.
43 M. Bahgat, A. A. Farghali, W. M. A. El Rouby and M. H. Khedr, *J. Anal. Appl. Pyrolysis*, 2011, **92**, 307–313.
44 A. Pozefsky and N. D. Coggeshall, *Anal. Chem.*, 1951, **23**(11), 1611–1619.
45 A. Ragunathan, R. Krishnan and B. Ameen, *J. Chem. Res.*, 2015, **39**, 622–626.
46 S. Her and C. Lai, *Materials*, 2013, 2274–2284.
47 A. Sinha, V. Nand, B. Raj and S. Kumar, *J. Hazard. Mater.*, 2011, **192**, 620–627.
48 A. Bayu, D. Nandiyanto, R. Ragadhita and M. Fiandini, *IJoST*, 2023, **8**, 113–126.
49 H. C. A. Murthy, C. H. Prakash and B. Abebe, *Current Research in Science and Technology*, 2020, vol. 4, pp. 113–131.
50 S. Haq, S. Dildar, M. Ben Ali, A. Mezni, A. Hed and M. I. Shahzad, *Mater. Res. Express*, 2021, **8**(5), 055006.
51 S. Haq, F. Abbasi, M. Ben Ali, A. Hed, A. Mezni and W. Rehman, *Mater. Res. Express*, 2021, **8**(7), 075009.
52 A. K. Abbas, S. K. Abass and A. M. Bashi, *MSE*, 2019, **571**, 012067.
53 A. Iqbal, A. Haq, G. Antonio, S. Ali, R. Naqvi, P. Westerhoff and S. Garcia-segura, *Catalysts*, 2021, **11**(7), 806.
54 T. Oh, *Bull. Korean Chem. Soc.*, 2009, **30**, 0–3.
55 A. Manjunath, M. Irfan and K. P. Anushree, *Adv. Mater. Phys. Chem.*, 2016, 263–273.
56 B. El-ghmari, H. Farah and A. Ech-chahad, *Bull. Chem. React. Eng. Catal.*, 2021, **16**, 651–660.

57 M. B. Ali, K. Elmnasri, S. Haq, S. Shujaat, M. Hfaiedh and F. B. Abdallah, *Dig. J. Nanomater. Biostruct.*, 2023, **18**, 1577–1585.
58 P. L. Meena, K. Poswal, A. K. Surela and J. K. Saini, *Water Sci. Technol.*, 2021, **84**, 2615–2634.
59 N. O. Photocatalysis, O. Al-madanat, B. N. Nunes, Y. Alsalka, A. Hakki, M. Curti, A. O. T. Patrocinio and D. W. Bahnemann, *Catalysts*, 2021, 1514.
60 V. Polliotto, S. Livraghi and E. Giamello, *Res. Chem. Intermed.*, 2018, **44**, 3905–3921.
61 V. D. Pakhale and P. R. Gogate, *Arabian J. Sci. Eng.*, 2021, 6473–6484, DOI: **10.1007/s13369-020-05074-5**.
62 D. Mahale, S. P. Hinge and B. S. Banerjee, *Desalin. Water Treat.*, 2016, 18275–18285.
63 U. G. Akpan and B. H. Hameed, *J. Hazard. Mater.*, 2009, **170**, 520–529.
64 D. M. Nzilu, E. S. Madivoli, D. S. Makhanu, S. I. Wanakai, G. K. Kiprono and P. G. Kareru, *Sci. Rep.*, 2023, **13**, 14030.
65 S. Haq, H. Afsar, I. U. Din, P. Ahmad, M. U. Khandaker, H. Osman, S. Alamri, M. I. Shahzad, N. Shahzad, W. Rehman and M. Waseem, *Catalysts*, 2021, **11**, 1–15.
66 J. Ren, Y. Z. Wu, Y. Dai, D. W. Sha, M. Chen, J. J. Wang, J. M. Pan, H. Tang, X. N. Cheng and X. H. Yan, *Mater. Technol.*, 2017, **32**, 574–583.
67 B. Siripireddy and B. K. Mandal, *Adv. Powder Technol.*, 2017, **28**, 785–797.
68 M. A. El-Bindary, M. G. El-Desouky and A. A. El-Bindary, *Appl. Organomet. Chem.*, 2022, **36**, 1–16.
69 M. Afifi, O. A. Almaghrabi and N. M. Kadasa, *BioMed Res. Int.*, 2015, 1–6, DOI: **10.1155/2015/153573**.
70 A. Hamid, S. Haq, S. Ur Rehman, K. Akhter, W. Rehman, M. Waseem, S. Ud Din, Z.-u. Abdin, M. Hafeez, A. Khan and A. Shah, *Chem. Pap.*, 2021, **75**, 4189–4198.
71 S. A. Bhat, F. Zafar, A. H. Mondal, A. Kareem, A. U. Mirza, S. Khan, A. Mohammad, Q. M. R. Haq and N. Nishat, *J. Iran. Chem. Soc.*, 2020, **17**, 215–227.